Analysis of anisotropic damage in forged Al–Cu–Mg–Si alloy based on creep tests, micrographs of fractured specimen and digital image correlations

Elisabetta Gariboldi [a], Konstantin Naumenko [b,n], Oksana Ozhoga-Maslovskaja [a], Emanuele Zappa [a]

[a] Politecnico di Milano, Department of Mechanical Engineering, Via La Masa 34 20156 Milano, Italy
[b] Otto-von-Guericke-University Magdeburg, Institute of Mechanics, D-39106 Magdeburg, Germany

ABSTRACT

The aim of this paper is to analyze anisotropic damage mechanisms in forged Al–Cu–Mg–Si alloy based on the results of creep tests. Smooth specimens are sampled in three forging directions. Creep strain vs. time curves as well as light optical microscope and scanning electron microscope observations illustrate basic features of damage growth. Flat notch specimens are sampled in different directions to analyze stress redistributions and damage in zones of stress concentration. The digital image correlation tech-nique has been applied in situ in order to extract the strain values on the surface of the notched spe-cimens. All observations demonstrate that the principal origins of anisotropic creep and damage are associated with elongated grains and second phase clustered particles located at grain boundaries. Longitudinal specimens possess nucleations of decohesion sites and growth of voids around second phase particles at grain boundaries. Damage evolution for radial and transverse specimens is due to the formation and growth of cracks in second phase particles orthogonal to the principal stress axis. Residual strains are confined to the notch root as well as to the flanges of advanced macrocrack, indicating the small scale yielding during the creep fracture process.

Keywords:
Al–Cu–Mg–Si alloy
Elongated grains
Creep damage
Notched specimen
Creep crack growth
Digital image correlation

1. Introduction

Age-hardenable AA2xxx alloys based on the aluminum–copper system exhibit superior creep strength and are widely used in structural components operating at elevated temperatures [1,2]. Complex shape parts produced from these alloys usually possess microstructural anisotropy as a result of processing [3]. Furthermore, the creep properties of age-hardenable alloys strongly depend on the heat treatment and ageing conditions [4].

In order to capture hot deformation processes as well as for the analysis of structures operating at high temperature, experimental data for the material response under different loading conditions is required. In addition, analysis of changes in microstructure accompanying deformation, such that coarsening of particles, nucleation and growth of cavities and other processes leading to softening and damage are of primary importance. Experimental data for the creep response as well as data on microstructural evolution are the basis for the development of constitutive models for inelastic deformation. Basic approaches to develop a constitutive model as well as the experimental data required for the identification are discussed in [5–7], for various materials.

Hardening/recovery, ageing and damage processes in aluminum alloys are widely documented in the literature. In [8] a phenomenological model is developed with hardening, ageing and damage parameters to capture creep of the aluminum alloy BS 1742 at 150 °C. A similar model is developed and applied to the analysis of creep age forming processes in [9]. The material parameters are identified for alloys AA2324 and AA7B04. In [10–12] the mean dislocation density and the characteristic particle size are used as internal state variables to characterize Taylor-type dislocation hardening and Orowan-type precipitation hardening mechanisms in various aluminum alloys.

Tertiary creep is usually described by damage, overageing and/or softening variables and corresponding evolution equations. In [13,14] a single damage state variable is utilized to reflect all processes leading to the tertiary creep stage. In [8,9] two independent state variables and kinetic equations are introduced to capture overageing and cavitation processes. A constitutive model

Article history:
Received 11 November 2015
Received in revised form 27 November 2015
Accepted 28 November 2015
Available online 30 November 2015

* Corresponding author.
E-mail addresses: elisabetta.gariboldi@polimi.it (E. Gariboldi), konstantin.naumenko@ovgu.de (K. Naumenko), oksana.ozhogamaslovskaja@gmail.com (O. Ozhoga-Maslovskaja), emanuele.zappa@polimi.it (E. Zappa).

Published Journal Article available at: http://dx.doi.org/10.1016/j.msea.2015.11.090

of anisotropic creep for a forged Al–Cu–Mg–Si alloy is developed in [15] taking into account elongated grains observed in the microstructure. A phase mixture approach is applied to describe stress redistributions in microstructural zones observed for different loading directions. The presence of intragranular strengthening particles is considered and the evolution equation for the normalized particle size is proposed to characterize hardening/recovery and overageing processes.

Experimental data for Al–Cu–Mg–Si alloy including tensile and creep curves for different forging directions are presented in [15,16,4,3]. The aim of this paper is to analyze anisotropic damage mechanisms in Al–Cu–Mg–Si alloy based on the results of creep tests. Smooth specimens are sampled in three forging directions. Creep strain vs. time curves as well as light optical microscope (LOM) and scanning electron microscope (SEM) observations illustrate basic features of damage growth. Flat notch specimens are sampled in different directions to analyze stress redistributions and damage in zones of stress concentration. For a proper design of notched specimens finite element analysis is performed by taking into account anisotropic creep. Creep strength curves are presented to assess the influence of notches on the lifetime. Results of LOM and SEM observations are presented to discuss damage mechanisms in the notch root zone. The digital image correlation (DIC) technique has been applied in situ in order to extract the strain values on the surface of the notched specimens. Time-dependent strain fields are presented to illustrate strain concentrations in the notch zone as well as in the zones confined to fracture surfaces. The results of DIC measurements are compared with those based on the finite element analysis.

2. Experimental details

The material investigated is an Al–4.4Cu–0.5Mg–0.9Si–0.8Mn alloy (IADS 2014 grade). An extruded bar from this alloy was axisymmetrically forged to produce a cave cylinder with the length of 230 mm and an external diameter of 190 mm. Let us designate three directions of a cylindrical forging as follows: the longitudinal (axial) by *L*, the tangential (circumferential) by *T* and the radial by *R*.

2.1. Smooth samples

Al–Cu–Mg–Si alloy forging had displayed anisotropic effects in *L*, *T* and *R* sampling directions [17]. Two sets of $20 \times 20 \times 100$ mm^3 bars were sampled from the as supplied forging with their longer side in *L* and *T* directions, respectively. Tension tests were performed at temperatures within the range 20–170 °C. Creep tests were conducted under constant load at 130 °C, 150 °C and 170 °C (homologous temperature range 0.44–0.49) under stresses that led to a range of times to rupture t_* from several hours to more than 10,000 h. Crept specimens were diametrally cut in order to investigate microstructure features along the gauge length.

2.2. Notched samples

Flat notched specimens were designed according to the type of creep testing machine and the grid system. The lateral dimensions of the specimen including grid parts were limited by the ratio 22×35 mm. The gauge width was 14 mm and the notch length was 5 mm. Two values of the notch radii have been chosen as 2.5 and 1.0 mm to reproduce a wide range of stress concentration. The sketch of the specimen with 2.5 mm notch radius is presented Fig. 1. To analyze the anisotropic effects of creep and damage notched specimen were sampled in *L* and *R* directions.

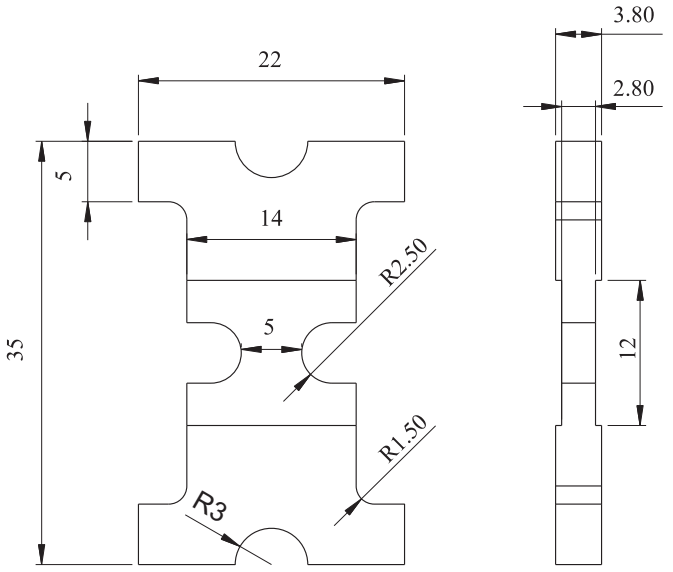

Fig. 1. Sketch of specimen with 2.5 mm notch radius. All dimensions are given in mm.

Notched specimen should be designed to assure that the material creeps at the notch rot and to avoid creep in shoulders. Furthermore, too high stress levels at the notch root would result in excessive deformation outside the power law creep regime, while too low stress values at the beginning and the subsequent stress redistribution would result in a prolonged test duration up to the fracture. For a proper design of notched specimen finite element simulations were performed by varying the geometry and the loading conditions.

One of the flat surfaces of every notched specimen was prepared for microstructural observations with SEM. To this end the notched part was cut from the entire specimen. The outer surface was used for experimental observations, carried out after mounting on the thermosetting resin and mechanical polishing. To reveal the microstructural features such as grain boundaries, precipitates and particles, the specimens were chemically etched with Keller's solution. The etching procedure as recommended for aluminium wrought alloys in [18] was applied.

2.3. Experimental setup for DIC

DIC is a vision-based measurement technique for full field strain estimation. It has been established in 1980s, e.g. Sutton et al. [19] and extensively developed within the last 30 years. In recent years DIC is widely used due to the progress in optical recording technique, promoting the accuracy and quality of acquisition. The basic idea is to compare a digital image of the surface at certain instant of loading with a reference image, taken before the testing. In order to perform a comparison the surface should possess a texture of the natural or artificial origin.

Depending on the imaging devise two types of DIC techniques can be distinguished:

1. 2D based on monocular device,
2. 3D or stereo, using two cameras.

The procedure of DIC consists of the following steps:

1. preparation of the specimen surface (application of texture),
2. image acquisition during the test,
3. digital image processing by means of DIC software to estimate

the strain field.

The requirements for the measurement surface for 2D or 3D correlation techniques are the same: clear and small enough patterns to track the strain gradient of expected magnitude with the constant background [20]. Different techniques are available in the literature to generate the speckle for DIC [21]. In this work, the geometry of used notched specimen, Fig. 1 is favorable for the application of DIC. Since the surface of the interest around the notch is flat and smooth, the simple speckle pattern transfer by means of air brush pen (similar to the one described in [22]) was sufficient. In order to increase the contrast between the speckle pattern and background, the specimens were covered by white inks, and after the drying the black ink speckle pattern has been applied. Furthermore the white uniform ink layer serves to avoid "shiny" surface, sensitive to the light reflection.

The specimens with the prepared surface were placed in furnace for 1 week at 150 °C in order to check if any distortions of the pattern can be caused by the applied temperature. It was found that the speckle on the specimen did not show any appreciable degradation during the time in the furnace. Moreover, the DIC software computes the uncertainty linked to the DIC results. The estimated uncertainty did not increase appreciably even after the permanence of the specimen at the temperature of 150 °C for 1 week, demonstrating that the pattern was not damaged. The example of obtained speckle pattern for the specimen with the notch radius of 2.5 mm is presented in Fig. 2.

In the case of 2D DIC out-of-plane motion changes the magnification and leads to an offset in the estimated strain fields. In this work the images for 2D DIC were acquired by a microscope for metallographic inspection, equipped with a specimen holder that allowed to accurately reposition the specimen on the microscope before and after the creep test, so that the effect of possible out of plane motion is minimized. To overcome completely the problem of out of plane motion the use of 3D DIC is recommended. Therefore the DIC tests with specimen mounted on the creep machine were done using a 3D DIC technique. The 3D technique requires more sophisticated experimental set up. The basic principles are described in detail by Schmidt et al. [23].

In the case of 2D DIC even small out-of-plane motion changes the magnification and leads to errors of measurements. To overcome this the use of 3D DIC is recommended. The 3D technique requires more sophisticated experimental set up. The basic principles are described in detail by Schmidt et al. [23].

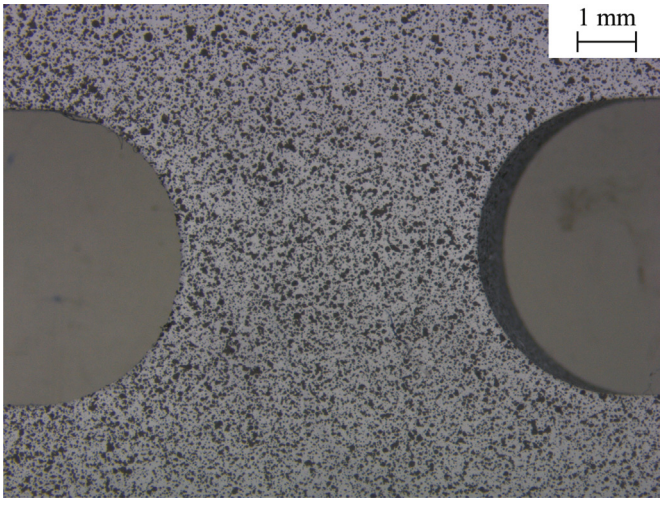

Fig. 2. Example of the textured surface of the specimen with a notch radius of 2.5 mm.

The images for 2D DIC were acquired with a stereo microscope equipped with a digital camera on one optical path, while the images for 3D DIC were acquired with two synchronized cameras. The 3D technique was applied leaving the specimen in its loading train in a creep machine equipped with a furnace that can be opened to take images in situ by two synchronized cameras. In order to allow the optical access to the cameras it was necessary to open the furnace. This leads to a drop in the temperature of the specimen. The effect of this temperature drop will be analyzed in the next section. The image acquisition stage was carried out applying the 3D technique that could guarantee better accuracy in particular for small out-of plane displacements.

The cameras used are Allied GX3300 digital cameras, equipped with a 3296 × 2472 px CCD sensor and a Ziess Makro-Planar $T \times 100$ mm optics with 100 mm focal length. The acquisition system is fully controlled by a software developed in LabVIEW that allows the configuration of the cameras, the image acquisition and storage of images. The DIC images were processed with the software suite VIC-3D from Correlated Solutions, Inc.

3. Results and discussion

3.1. Microstructure

The investigated forging was characterized by grains elongated in the main plastic flow path experienced during the processing. Their mean size of grains was about 300, 80 and 50 μm along the *L*, *T* and *R* directions, respectively. Fig. 3 shows light optical microscope micrographs of the microstructure of the forged part in 2014 alloy in different metallographic sections. Two kinds of coarse intermetallic particles were present in the microstructure: globular Al_2Cu (θ) particles (bright particles in Fig. 3) and blocky shaped clustered particles containing Fe, Mn, Si and Cu (darker particles in Fig. 3). These latter secondary phase clustered particles are elongated in the *L* direction. In most of the volume of the forging, macrographic analyzes revealed the large intermetallic particles longitudinally oriented, suggesting the same direction of the plastic flow during the processing.

In addition, transmission electron microscopy images published in [24] illustrate the presence of θ' phase, in the form of plate-like precipitates in {100} crystallographic planes of the α-Al matrix. These precipitates play an important role in strengthening of the alloy. The forging was supplied in the T6 condition, that is the solution treatment at 778 K and aging at 433 K for 16 h. During the subsequent creep overageing processes take place leading to the increase of particles size and distance between particles with time.

3.2. Minimum creep rates

Creep curves of the material sampled in *L* and *T* directions are presented and analyzed in [15]. Fig. 4 shows minimum creep rate vs. stress curves. To normalize the data the reference stress $\sigma_0 = 320$ MPa, the reference strain rate $\dot{\varepsilon}_0 = 1.026$ 1/h and the Arrhenius function of the temperature

$$f(T) = \exp(-\frac{Q}{RT}) \tag{1}$$

with apparent activation energy *Q*, the universal gas constant *R* and absolute temperature *T* is applied. The obtained value $Q = 175.42$ kJ/mol is consistent with the data published in [4,15]. The reference stress σ_0 is introduced to split the ranges of power law creep and power law breakdown, as shown in Fig. 4. According to experimental data presented in Fig. 4 the anisotropy is primarily observable in the power law range. The relation with the creep

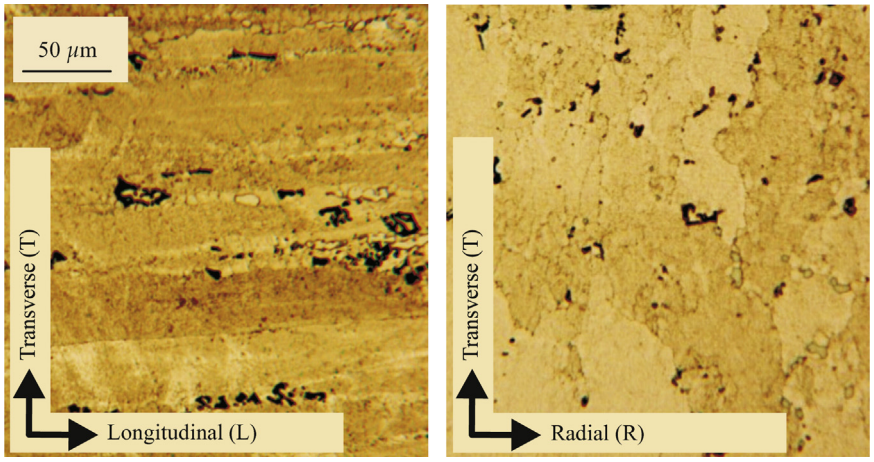

Fig. 3. Light optical microscope micrographs of the forged part from AA2014 in different metallographic sections.

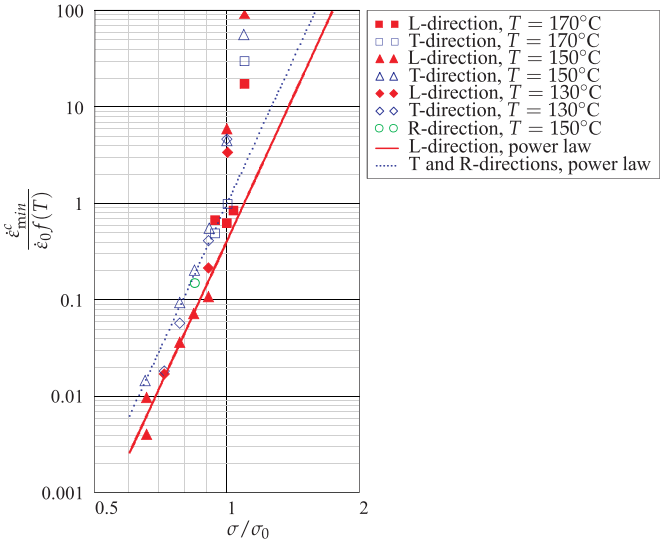

Fig. 4. Normalized minimum creep rate vs. normalized stress for longitudinal, transverse and radial creep tests of AA2014 at 150 °C.

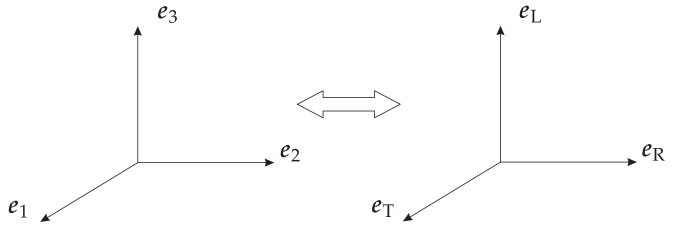

Fig. 6. Correspondence between local basis vectors defined in Abaqus and material orientations of forging.

rates

$$\dot{\varepsilon}^c_{T_{min}} = \alpha \dot{\varepsilon}^c_{L_{min}}, \quad \alpha = 2.43$$

The creep rate in the T direction is 2.43 times higher that the creep rate in the L direction for the same stress level. In the power law breakdown range the difference between L and T data is not essential, if compared to the usual scatter of experimental data in the creep range, and can be neglected. The minimum creep rates for T-specimen can be described by the following equation:

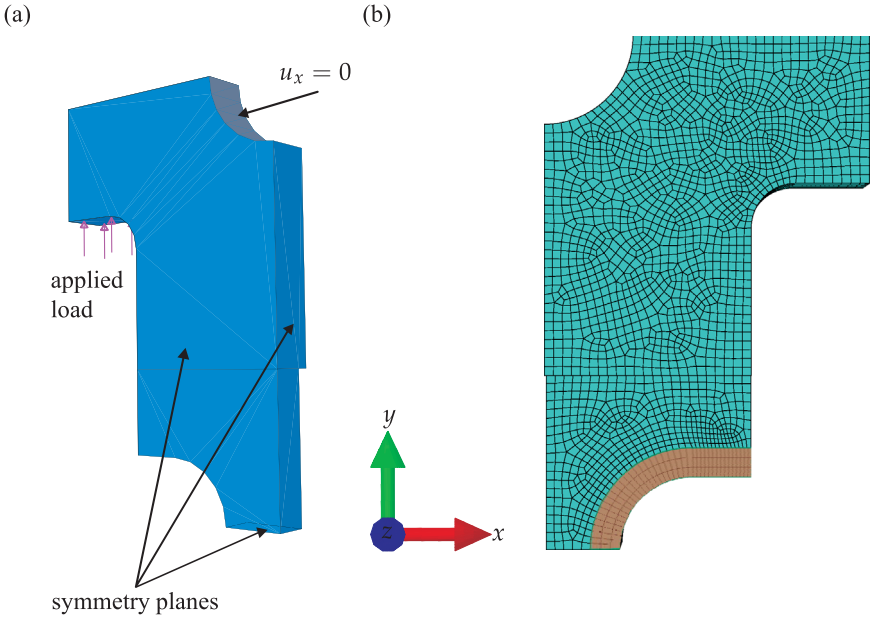

Fig. 5. Model of the specimen. (a) Geometry and boundary conditions and (b) finite element mesh.

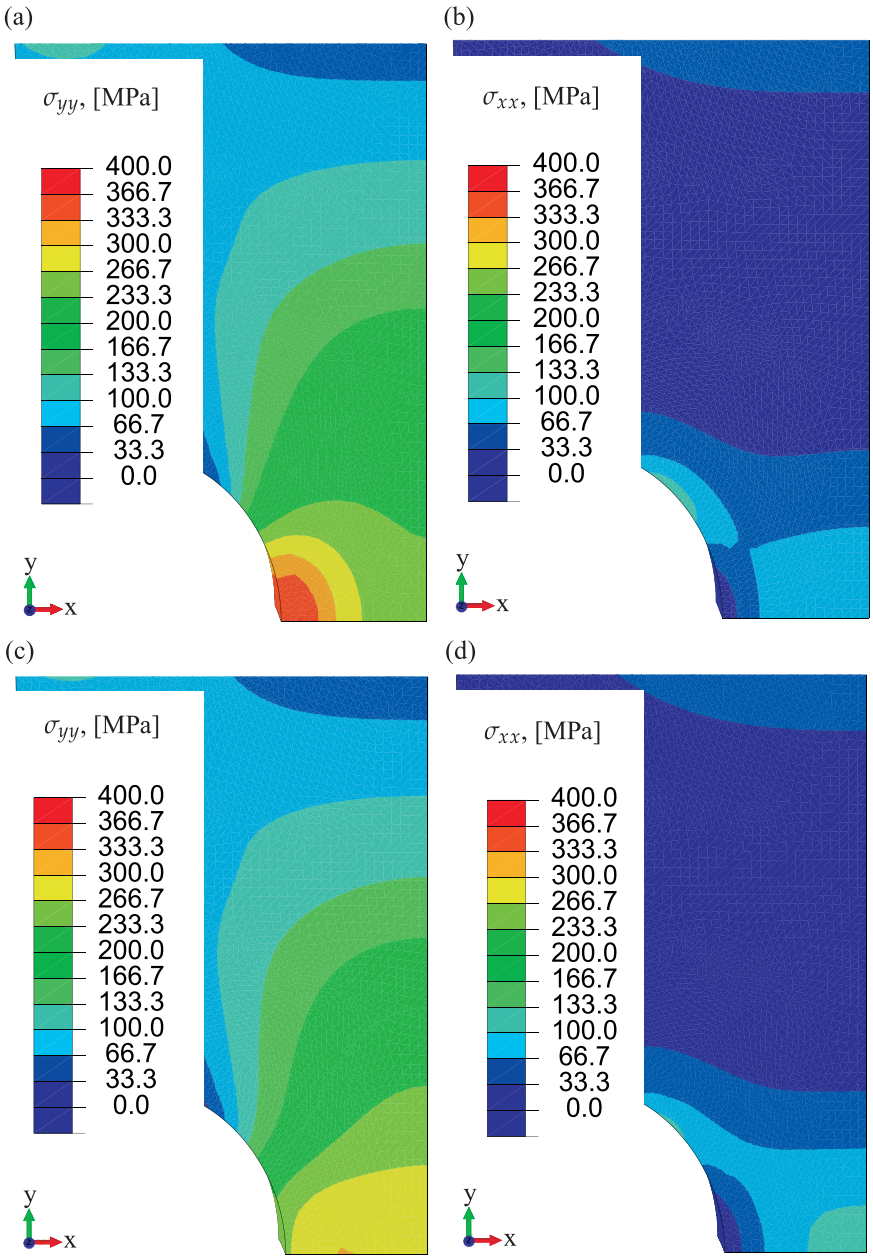

Fig. 7. Stress distributions around the notch of R-specimen sampled with a notch radius of 1 mm and net stress 290 MPa. (a) σ_{yy}, after the loading, (b) σ_{xx}, after the loading, (c) σ_{yy}, 400 h, and (d) σ_{xx}, 400 h.

$$\dot{\varepsilon}^{c}_{T_{min}} = \dot{\varepsilon}_0 f(T)(\frac{\sigma}{\sigma_0})^n$$

with $n=9.94$. Two additional creep tests at 150 °C for specimens sampled in R direction were performed in this study. The results indicate that the difference in creep rates for T and R directions is not essential, Fig. 4. This supports the assumption of transversely isotropic creep made in [15].

3.2.1. Finite element analysis

The Abaqus code is applied to generate geometrical and finite element models. Taking into account geometrical and loading symmetries, 1/8 of the specimen with 3 symmetry planes are considered, Fig. 5. On the surface, defining contact of the specimen with a pin the displacements constraint condition $u_x=0$ is used. The pin is a part of loading train, connecting the specimen with extensometers and elongation reading devices. The pins were made of heat resistant steel, stiffer and more creep resistant than the Al alloy of specimens. Hence, the applied boundary condition reflects well the real interaction of the specimen with the pin. The displacements in y and z directions on the surface are left unconstrained. The uniform pressure is applied below the shoulder as illustrated in Fig. 5a. Quadratic brick elements with reduced integration are used to mesh the geometrical model. The selected element type supplies better accuracy of stress values, expected at notch root.

The material behavior is prescribed based on standard models of elasticity and creep available inside Abaqus. The isotropic elasticity is characterized by Young's modulus $E=70$ GPa at room temperature, $E=62.2$ GPa at temperature 150 °C and Poisson's ratio $\mu = 0.33$.

Transversely isotropic creep behavior is assumed since the creep rates for T and R directions are nearly the same. Models of transversely isotropic creep are presented and identified in

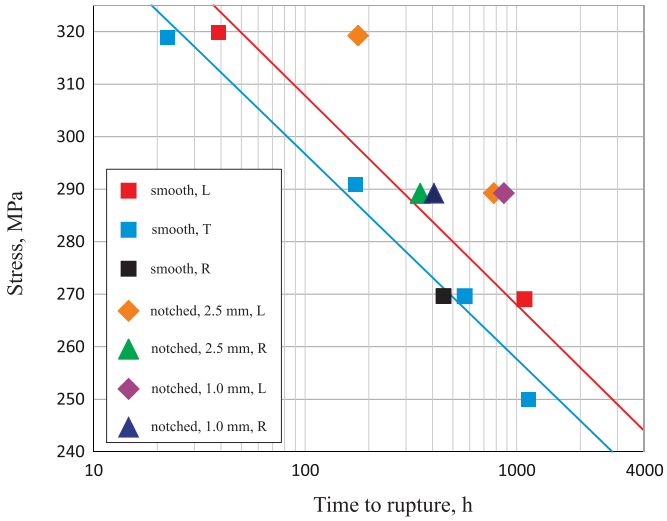

Fig. 8. Creep strength data for smooth and notched tensile specimens, sampled in L, T and R directions for $T = 150$ °C.

[25,26,15], among others for various materials. For the preliminary analysis of notched specimen let us ignore primary and tertiary creep stages and assume a power law secondary creep. In Abaqus Hill's potential is available to model orthotropic plasticity and creep [27] with the following stress ratios:

$$R_{11} = \frac{\sigma_{11}}{\tilde{q}}, \quad R_{22} = \frac{\sigma_{22}}{\tilde{q}}, \quad R_{33} = \frac{\sigma_{33}}{\tilde{q}}, R_{12} = \frac{\sigma_{12}}{\tilde{q}/\sqrt{3}}, \quad R_{13} = \frac{\sigma_{13}}{\tilde{q}/\sqrt{3}}, \quad R_{23} = \frac{\sigma_{23}}{\tilde{q}/\sqrt{3}} \tag{2}$$

The equivalent stress $\tilde{q}$ is defined as follows:

$$\tilde{q}(\boldsymbol{\sigma}) = \sqrt{F(\sigma_{22}-\sigma_{33})^2 + G(\sigma_{33}-\sigma_{11})^2 + H(\sigma_{11}-\sigma_{22})^2 + 2L\sigma_{23}^2, + 2M\sigma_{31}^2 + 2N\sigma_{12}^2} \tag{3}$$

where F, G, H, L, M and N are constants to be identified from tests in different loading directions. To model anisotropic creep inside Abaqus, material orientation must be defined by means of the local coordinate system associated with the geometrical model. The local coordinate system with the basis vectors $\mathbf{e}_1$, $\mathbf{e}_2$ and $\mathbf{e}_3$ is specified to define T, R and L directions of forging, as illustrated in Fig. 6. Based on results of creep tests in L, T and R directions, Fig. 4, the stress ratios are set as follows:

$$R_{11} = 1, \quad R_{22} = 1, \quad R_{33} = 1.1 \tag{4}$$

Different cases of loading magnitude, notch geometry and material orientation with respect to the loading axis were analyzed. As an example, Fig. 7 illustrates the results of computations for the net stress (load over the minimum reference cross section) of 290 MPa the notch radius of 2.5 mm and under the assumption that the R direction coincides with the loading axis while the T direction is the thickness direction of the specimen. Distributions of normal stresses in two directions at the beginning (immediately after the loading), Figs. 7a and b, and at the time step of 400 h, Figs. 7c and d, are presented. The stress state in the notch roots is nearly uni-axial since the stress components in the thickness direction are small and can be neglected. On the other hand, the stress state along the symmetry axis connecting the notches is bi-axial. The significant relaxation and redistribution of stresses during the creep exposure can be observed. Therefore, for this example we expect the apparent notch hardening effect: the maximum stress in the notch root substantially decreases and attains the value which is lower than the net stress. Therefore, the lifetime of the notched specimen is expected to be longer than the lifetime of the smooth specimen subjected to the net stress value. The net stress is defined as the ratio between the applied load and the minimum specimen cross section. Another effect is related to the multi-axiality of the stress state: after the stress redistribution the maximum value of the stress component σ_{xx} becomes comparable with value of the axial stress σ_{yy} along the line connecting the notches. This effect will be important in analysis of damage mechanisms.

3.3. Creep strength data

Fig. 8 shows creep strength data (stress vs. time to rupture) for specimens sampled in different directions. For the considered stress range the data for smooth specimens can be approximated by linear functions in a double logarithmic scale. The lifetime of

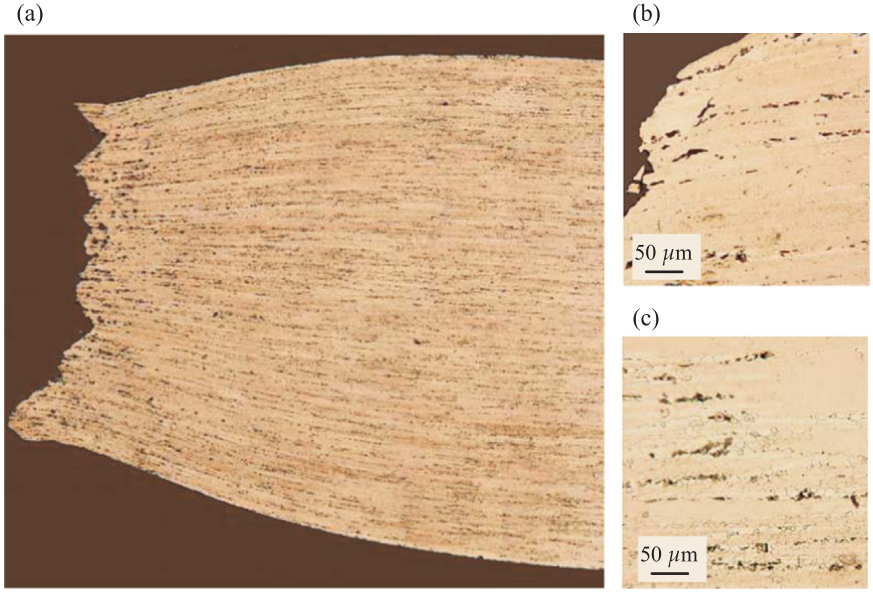

Fig. 9. LOM macrographs of crept specimen in L direction, $T = 170$ °C, $t_* = 336$ h. (a) Specimen, (b) magnification close to the rupture surface, and (c) magnification 2 mm away from the rupture surface.

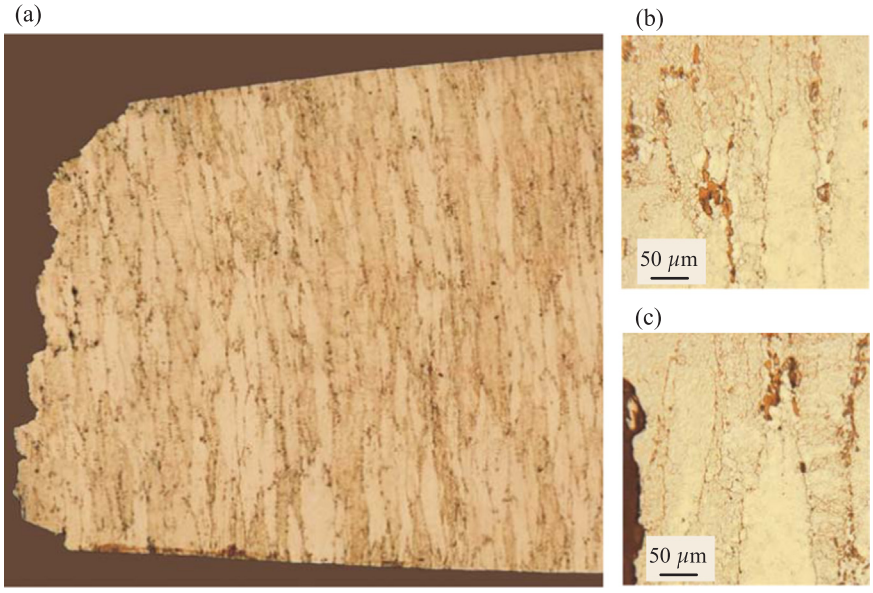

Fig. 10. LOM macrographs of crept specimen in *T* direction, $T = 130\ ^{\circ}C$, $t_* = 474$ h. (a) Specimen, (b) magnification close to the rupture surface, and (c) magnification two millimeters away from the rupture surface.

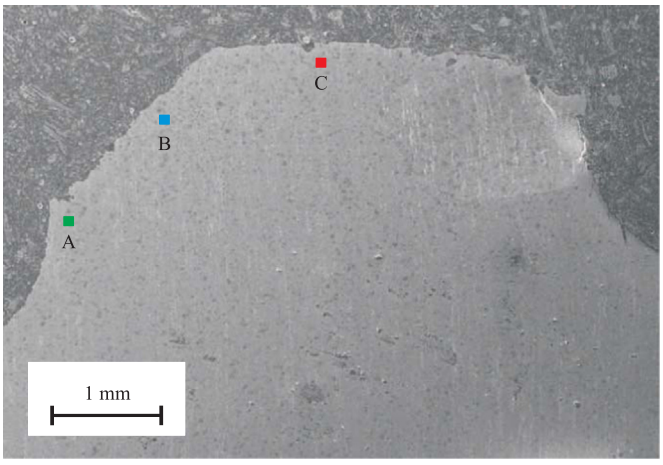

Fig. 11. SEM micrograph of fracture surface of L-specimen with a notch radius of 1.0 mm

smooth L specimens is approximately 2 times longer than the lifetime of T or R specimen for the same stress and temperature levels. Approximately the same difference in the lifetime is observed for L and R notched specimens tested under the same stress level and for the same notch radius. All notched specimens tested under the net stress of 290 MPa show the apparent notch hardening effect. This is consistent with the results of finite element simulations, where essential stress redistribution for specimen sampled in different directions was established.

3.4. *Damage*

Creep damage was significantly affected by the presence of the intermetallic coarse phases, approximately aligned in *L* direction and located at grain boundaries. Fig. 9 illustrates LOM photographs of crept specimen for loading in *L* direction. For this loading decohesions were nucleated at interfaces of the intermetallic coarse particles with the matrix. During the creep exposure they are extended to most of the particle surface. Staring from these decohesion sites void formation, growth and coalescence on the boundary of elongated grains were observed. Fig. 10 shows LOM photographs of specimen loaded in *T* direction. It is evident that the fracture is intergranular with lower creep ductility and lower concentration of creep voids, if compared to the L specimen.

In [15] a composite model of inelastic deformation was applied to explain the anisotropic creep behavior. For the loading in *L* direction a stress redistribution between grain interiors and grain boundary regions is assumed as a result of different creep rates in different microstructural zones. On the other hand no essential changes in the microstructural stress state can be expected if the material is loaded in *T* or *R* direction. The grain interiors and the grain boundary zones are subjected to approximately the same stress levels during the creep exposure. As a result the difference in the overall creep rates is observed – T and R specimens exhibit higher creep rates than L specimen for the same overall stress level. Damage states observed in Figs. 9 and 10 can be closely related to processes of stress redistribution and deformation in different microstructural zones. Indeed, the stress increase is expected in the harder grain boundary affected regions for loading in *L*-direction. This leads to brittle fracture of intermetallic particles as well as subsequent decohesions. Growth and coalescence of voids lead to unloading of the initially creep harder regions and to additional stress redistribution providing higher stress level and the higher creep rate in the matrix. This process would promote the necking instability and the final fracture. On the other hand, for T or R specimen grain interiors and grain boundary zones are subjected to nearly the same stress levels. Therefore microcracks and decohesions around intermetallic particles are expected to nucleate and grow with higher rates if compared to L specimen. As a result, T and R specimens have shorter creep life, if compared to the L specimen for the same stress and temperature levels as well as reduced ductility. Fig. 11 shows the whole fracture profile of the L-specimen with the notch radius of 1.0 mm and tested under the net stress of 290 MPa. To investigate the damage type and distribution, SEM micrographs were taken at various magnifications, different positions and distances from the fracture surface. Figs. 12a–c show three micrographs taken at the distance of 150 μm from the fracture surface. The corresponding zones A, B, and C are designated in Fig. 11. Microcracks within the secondary phase particles, decohesion sites and isolated voids can be recognized.

Fig. 13 shows the whole fracture profile of the R-specimen with the notch radius of 1.0 mm and tested under the net stress of

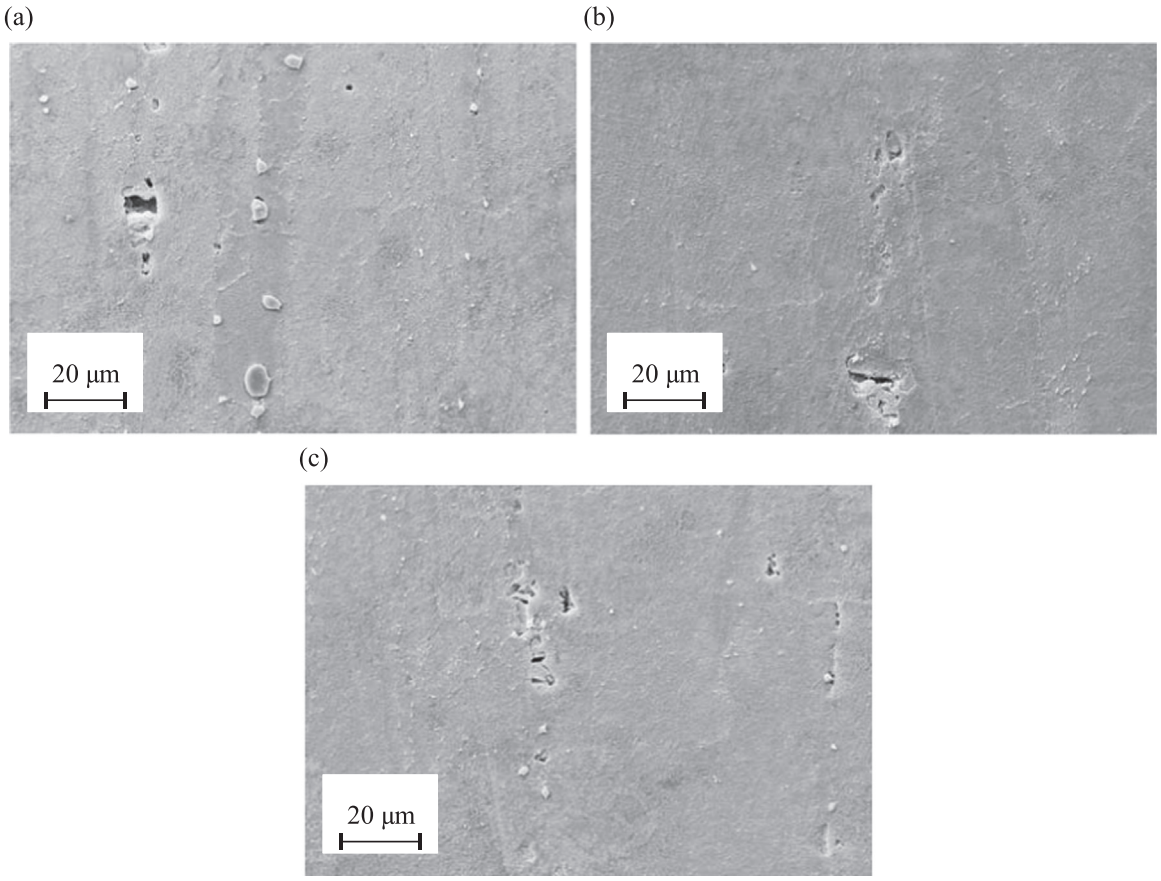

Fig. 12. SEM micrographs of different zones of the fracture surface for L-specimen. (a) 150 μm from fracture surface, zone A, magnification × 3000, (b) 150 μm from fracture surface, zone B, magnification × 3000, and (c) 150 μm from fracture surface, zone C, magnification × 3000. The zones A, B and C are presented in Fig. 11.

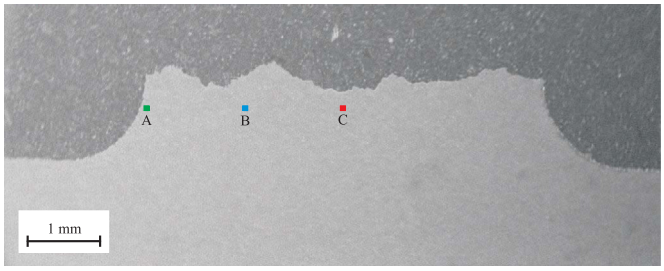

Fig. 13. SEM micrograph of fracture surface of R-specimen with a notch radius of 1.0 mm.

290 MPa. Three micrographs taken at the distance of 150 μm from the fracture profile in zones A, B, and C are presented in Fig. 14a–c. The corresponding locations are shown in Fig. 13. One may recognize oriented microcracks within the secondary phase particles in zone A close to the notch surface, Fig. 14a. In the zone C closer to the center, Fig. 14c, decohesions from the surrounding metallic matrix can be observed. An intermediate situation between these two damage forms has been observed in the zone B between the notch and the center of the specimen, Fig. 14b. This difference can be explained by the stress field along the line connecting the notches, predicted by the FE simulations.

Based on SEM observations and results of finite element simulations, the following scenario of damage evolution can be assumed. At the beginning of the creep process, brittle fracture of secondary phase particles occurs in the zones close to the notch root due to relatively high stress levels. During the creep exposure, stress redistribution takes place leading to a decrease of stress levels in the notch root and an increase of stress levels in ligaments. Here a typical creep damage mechanism, namely the decohesion of particles from the matrix along grain boundaries under moderate stress level, is observed.

For the L specimens micro-stress redistribution between grain interiors and grain boundary regions can be assumed as a result of different creep rates in different microstructural zones. In contrast, no microstress redistributions are expected for notched specimens sampled in *R*-direction. As a result notched L-specimens have longer creep life if compared to the R-specimens. Furthermore, as SEM-observations indicate, fracture of R-specimens is more brittle and mainly caused by microcracks oriented along the grain boundaries and orthogonal to the first principal stress axis.

3.5. *Strain fields*

Analysis of microstructure close to the fracture profile provides the information about the final damage state in the material. To give a more precise picture of creep process experimental data for strain vs. time behavior in different regions around the notch are helpful. To extract strain fields the digital image correlation technique (DIC) is applied.

A wide range of data for three-dimensional displacement and strain fields can be extracted after 3D DIC image processing. The schematic representation of the acquisition domain within the specimen surface is shown in Fig. 15.

Strain fields obtained by 2D DIC for the L specimen with 1.0 mm notch radius, applied net stress 290 MPa after the creep exposure of 910 hours are illustrated in Fig. 16. The results show that residual strains take considerable values only in the zone between the notches. In the “smooth” zone outside the stress concentration the residual strains are negligible. This indicates

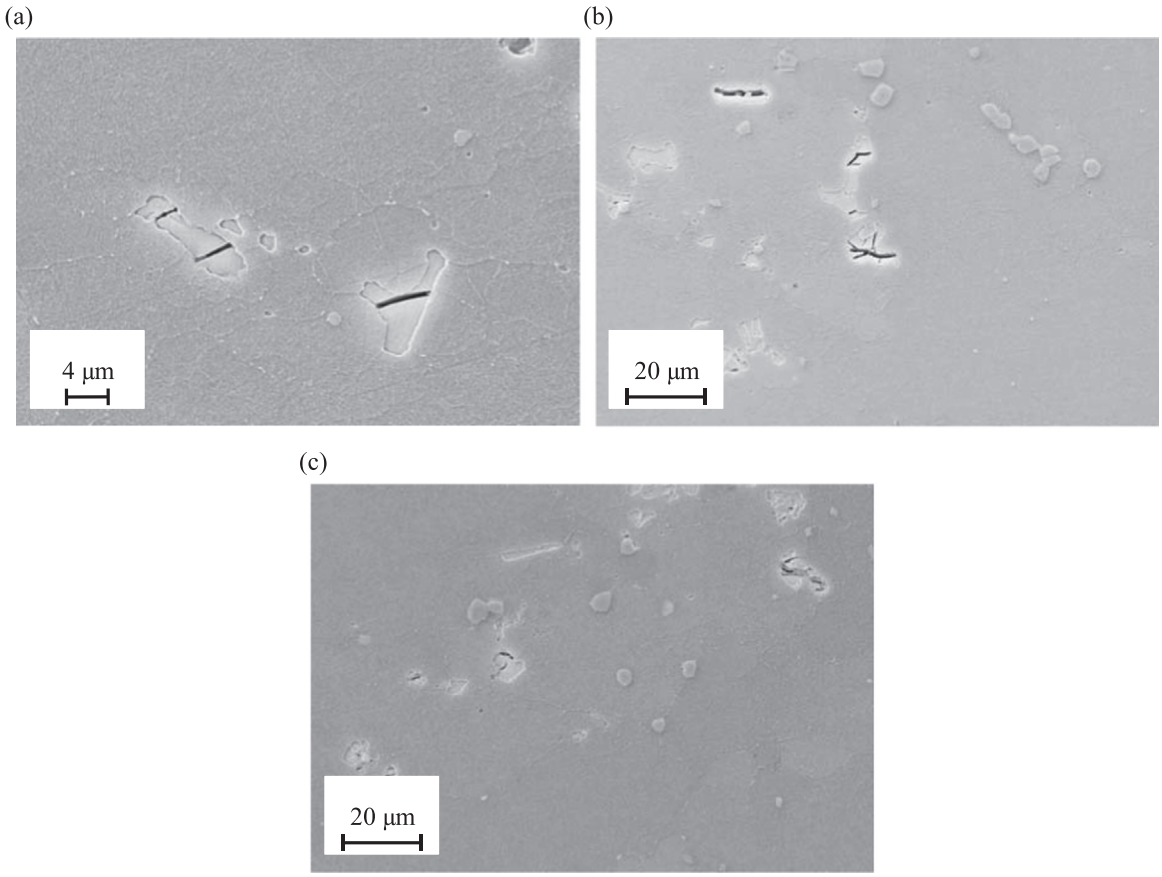

Fig. 14. SEM micrographs of different zones of the fracture profile for R-specimen. (a) 150 μm from fracture profile, zone A, magnification × 8000, (b) 150 μm from fracture profile, zone B, magnification × 3000, and (c) 150 μm from fracture profile, zone C, magnification × 3000. The zones A, B and C are presented in Fig. 13.

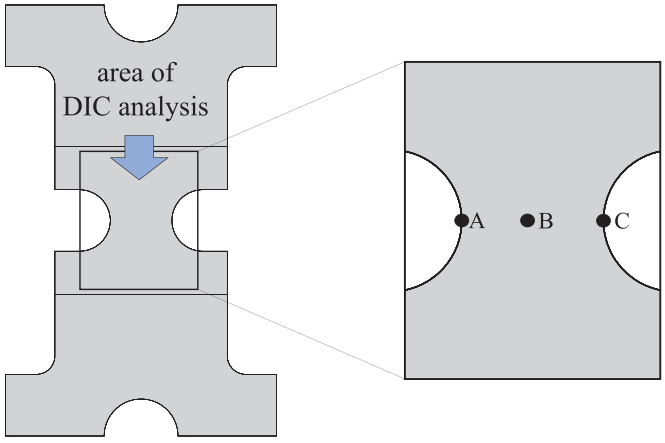

Fig. 15. Location of the DIC acquisition domain within the specimen surface. A, B and C are points on the line, connecting two notches.

that the creep deformation process was confined to the notches. This conclusion is consistent with the results of finite element analysis. Once a macrocrack is initiated in one of the notches, the symmetry of loading is lost leading to a non-symmetric crack path. Regions with localized residual strains in the neighborhood of the fracture surfaces can be recognized. This result indicates the small scale yielding around the crack tip during the fracture process.

Let us discuss the results of 3D DIC analysis for the specimen, sampled in *R* direction with the notch radius of 2.5 mm tested under a net stress of 290 MPa. First of all we need to estimate the accuracy associated with the thermal strain fields, caused by specimen cooling after the furnace opening, necessary for image acquisition. To this purpose, maintaining the mechanical loading fixed, the images of the specimen were acquired at 130 °C and 30 °C. The corresponding strain fields are shown in Fig. 17. The results are subtracted leading to the pure thermal strain distribution, Fig. 18. The thermal strain field is homogeneous. Furthermore the strain value divided by the temperature difference is consistent with the coefficient of thermal expansion $\alpha_T = 2.3{\cdot}10^{-6}1/\mathrm{K}$ known for this alloy.

Fig. 19 shows the distribution of strain ε_{yy} after 201 h of creep exposure and after 373 h at creep fracture. Similar to the L-specimen, the strain concentration is confined to the notch root. However, the maximum strain value is much lower. Furthermore relatively low strain values are observed in zones confined to crack flanges. This indicates a more brittle character of creep fracture for R-specimen.

To follow the strain evolution the data is collected for certain points of the specimen at different test times. Fig. 20 shows the results of DIC at three points A, B and C along the line connecting the notches. The locations of these points are presented in Fig. 15. Despite the fact that the specimen has symmetric shape, which ensures the symmetrical loading of both notches, DIC results show the obvious difference between the left and right notches. This can be explained by either a non-perfect alignment of the specimen at the gripping end, or by non-perfect alignment of the anisotropy axis with respect to the loading. The strains derived from DIC analysis are compared to those obtained from finite element analysis (dashed lines in Fig. 20). Note that the FE-model is symmetric providing the same strains in A and C. To compare results of simulations with experimental data the mean of the strains in A and C derived from DIC is computed. Despite the slightly non-

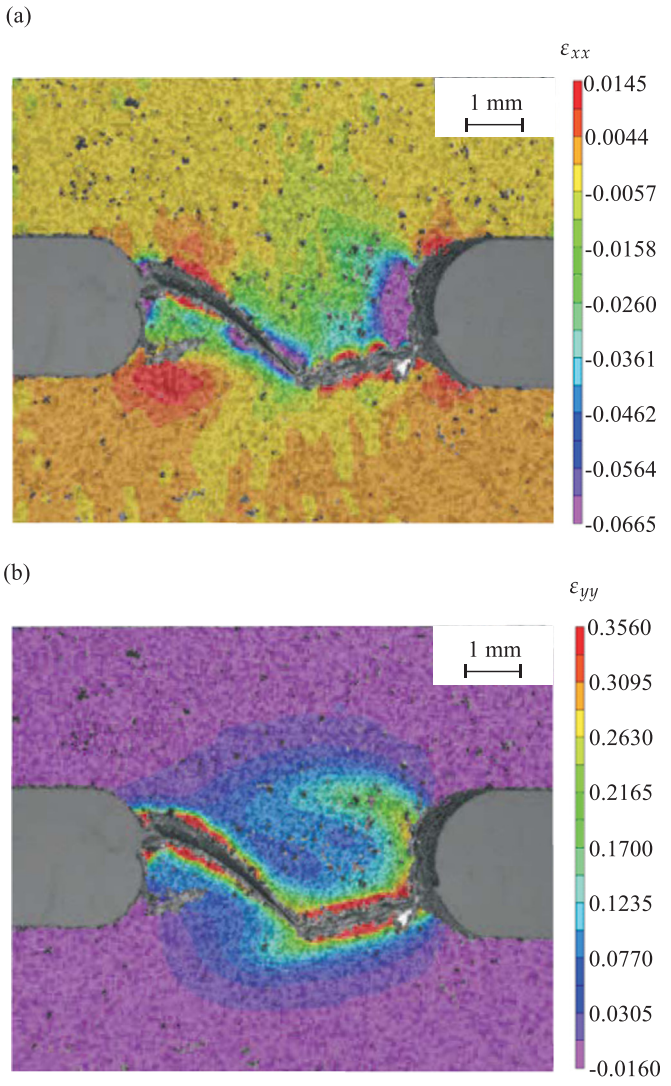

Fig. 16. Strain field around the notch of the L-specimen with radius of 1.0 mm crept at net stress 290 MPa and failed after 910 h. (a) ε_{xx} and (b) ε_{yy}.

symmetrical strain field obtained in test and the simplified anisotropic creep model used in simulations, the results agree well with respect to the usual scatter of creep measurements. One can see a good correlation between strains predicted by FE simulation and measured experimentally with the DIC.

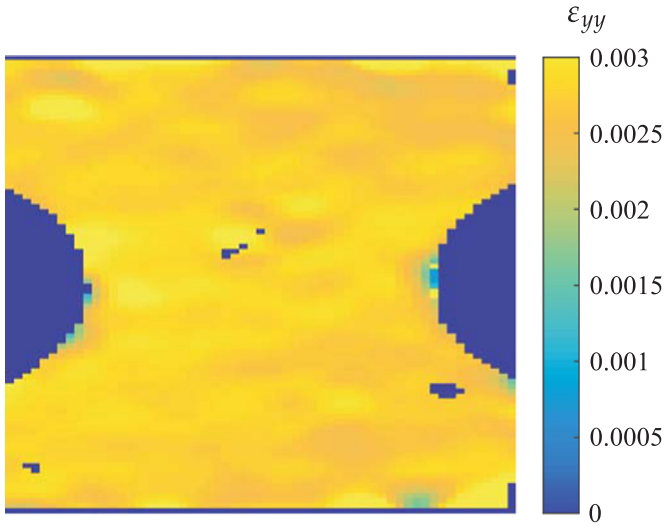

Fig. 18. Thermal strain field estimated by subtracting experimentally measured strain fields at 30 °C from 130 °C.

4. Conclusions

The aim of this paper was to analyze anisotropic damage in Al–Cu–Mg–Si alloy based on the results of creep tests on smooth and notched specimens. Based on the results we may conclude as follows:

- Minimum creep rate vs. time curves and stress vs. time to rupture curves for smooth and notched specimens sampled in *L* and *T* or *R* direction clearly illustrate anisotropic deformation and damage processes.
- The principal origins of anisotropic creep and damage are associated with elongated grains and second phase clustered particles located at grain boundaries.
- LOM and SEM photographs show basic features of anisotropic damage. L-specimens possess nucleations of decohesion sites and growth of voids around second phase particles at grain boundaries. Damage evolution for R or T specimens is due to the formation and growth of cracks in second phase particles orthogonal to the principal stress axis.
- DIC illustrate that residual strains are confined to the notch root as well as to the flanges of advanced macrocrack. This indicates the small scale yielding during the creep fracture process.
- Strain values around notches and in the vicinity of crack flanges clearly indicate anisotropic character of creep damage.

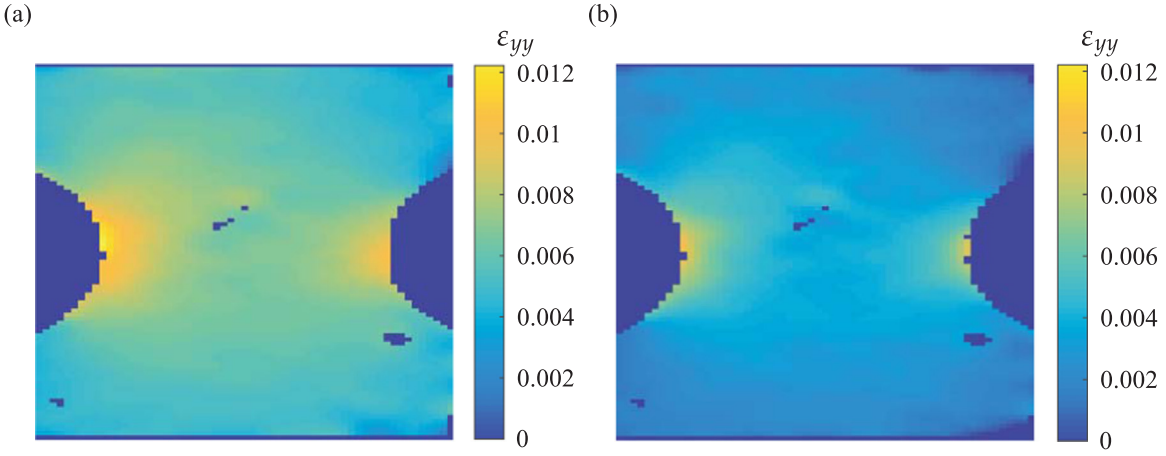

Fig. 17. Strain distributions on the surface of R-specimen, tested at 290 MPa and measured after 17.3 h at different temperatures. (a) 130 °C and (b) 30 °C.

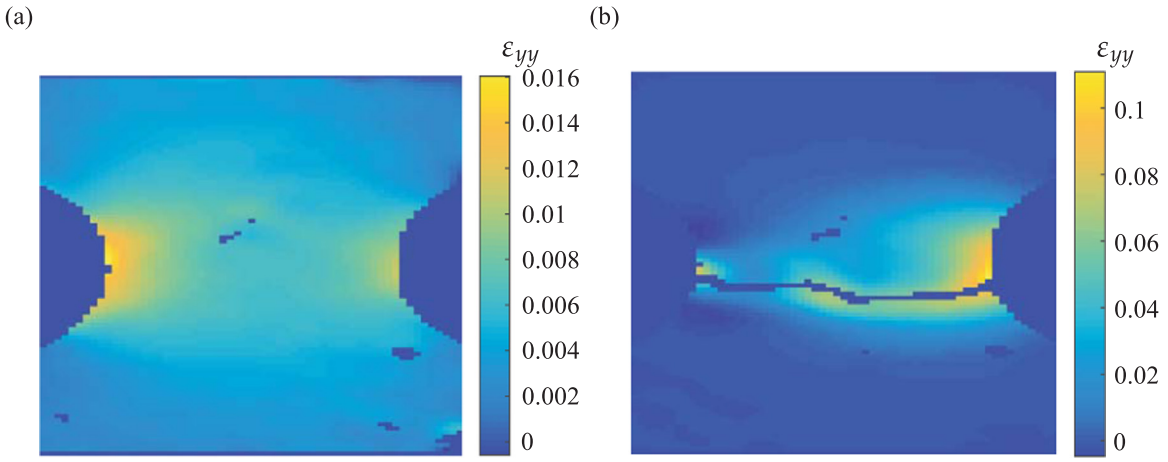

Fig. 19. Strain distributions on the surface of R-specimen tested at 290 MPa. (a) after 201 h and (b) after 373 h (fracture).

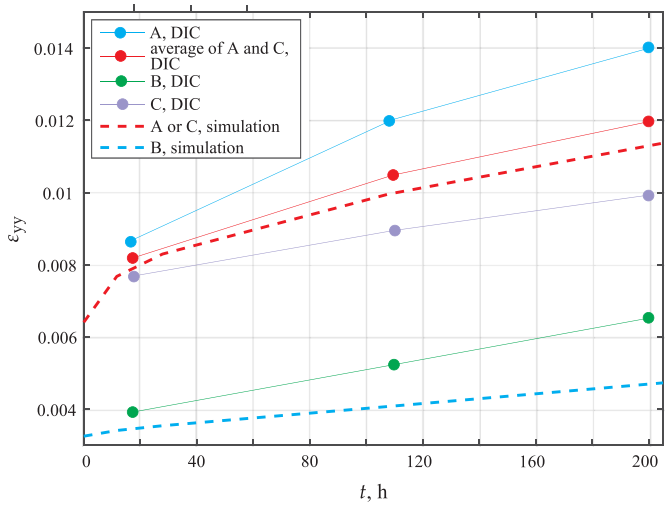

Fig. 20. Strain vs. time at different locations of the R-specimen. Experimental data from DIC and results of FE simulation.

R-specimens show much lower strain values in the strain concentration zones if compared to the L-specimens.

Observations presented in this paper are useful for the development of a model for anisotropic creep damage evolution. Experimental data on creep rates and fracture times can be used for the model calibration. Utilizing the developed creep damage model inside a finite element code would provide information on damage zones in components. Strain fields generated in this study for notched specimen based on DIC can be used to validate the developed creep-damage model and finite element simulations of creep damage and creep fracture processes.

References

[1] I.J. Polmear, Mater. Trans. JIM 37 (1996) 12–31.
[2] I.J. Polmear, Mater. Forum 28 (2004) 1–14.
[3] E. Gariboldi, A. Conte, in: Advanced Materials Modelling for Structures, Springer, Berlin, Heidelberg, 2013, pp. 165–175.
[4] E. Gariboldi, F. Casaro, Mater. Sci. Eng.: A 462 (2007) 384–388.
[5] J.L. Chaboche, Int. J. Plast. 24 (2008) 1642–1693.
[6] K. Naumenko, H. Altenbach, A. Kutschke, Int. J. Damage Mech. 20 (2011) 578–597.
[7] F. Längler, K. Naumenko, H. Altenbach, M. Ievdokymov, J. Strain Anal. Eng. Des. 49 (2014) 421–428.
[8] Z.L. Kowalewski, D.R. Hayhurst, B.F. Dyson, J. Strain Anal. Eng. Des. 29 (1994) 309–316.
[9] L. Zhan, J. Lin, T.A. Dean, Int. J. Mach. Tools Manuf. 51 (2011) 1–17.
[10] J. Dünnwald, E. El-Magd, Comput. Mater. Sci. 7 (1996) 200–207.
[11] E. El-Magd, A. Kranz, Materialwiss. Werkstofft. 31 (2000) 96–101.
[12] N. Anjabin, A. Karimi Taheri, Mater. Des. 31 (2010) 433–437.
[13] H. Altenbach, K. Naumenko, Comput. Mech. 19 (1997) 490–495.
[14] H. Altenbach, G. Kolarow, O. Morachkovsky, K. Naumenko, Comput. Mech. 25 (2000) 87–98.
[15] K. Naumenko, E. Gariboldi, Mater. Sci. Eng.: A 618 (2014) 368–376.
[16] E. Gariboldi, D. Ripamonti, L. Signorelli, G. Vimercati, F. Casaro, Metall. Sci. Tecnol. 25 (2003) 3–11.
[17] E. Gariboldi, A. Lo Conte, Advanced materials modelling for structures in: H. Altenbach, S. Kruch (Eds.), Advanced Structured Materials, vol. 19, Springer, Berlin, Heidelberg, 2013, pp. 165–175.
[18] G.F. Vander Voort, Metallography Principles and Practice, ASM International, USA, 1999.
[19] M.A. Sutton, W.J. Wolters, W.H. Peters, W.F. Ranson, S. McNeill, Image Vis. Comput. 1 (1983) 133–139.
[20] P. Mazzoleni, F. Matta, E. Zappa, M.A. Sutton, A. Cigada, Opt. Lasers Eng. 66 (2015) 19–33.
[21] P. Mazzoleni, E. Zappa, F. Matta, M.A. Sutton, Opt. Lasers Eng. 75 (2015) 72–80.
[22] A. Garghentini, A. Silvestri, B. Rivolta, E. Zappa, J. ASTM Int. 9 (2011) 1–9.
[23] T. Schmidt, J. Tyson, K. Galanulis, Exp. Tech. 27 (2003) 22–26.
[24] A. Angella, E. Bassani, E. Gariboldi, D. Ripamonti, in: J. Hirsch, B. Skrotsky, G. Gottstein (Eds.), Aluminium Alloys, vol. 1, Wiley-VCH, Weinheim, 2008, pp. 1092–1067.
[25] J. Betten, Creep Mechanics, Springer, Berlin, Heidelberg, 2008.
[26] K. Naumenko, H. Altenbach, Arch. Appl. Mech. 74 (2005) 808–819.
[27] ABAQUS, Analysis User's Manual, Dassault Systèmes Simulia Corp., USA, 2009.